

REGULAR PAPER
2022 ISABE Conference Paper

Performance of a turbojet engine with fluidic thrust vectoring

T. Chandra Sekar , R. H. Sundararaj* , R. Arora  and A. Kushari 

Department of Aerospace Engineering, Indian Institute of Technology Kanpur (IITK), Kanpur, Uttar Pradesh, India
*Corresponding Author. Email: ramraj@iitk.ac.in

Received: 29 October 2021; **Revised:** 11 January 2022; **Accepted:** 28 February 2022

Keywords: Thrust vector control; Gas turbine performance; Fluidic thrust vectoring

Abstract

The objective of the present work is to estimate the performance of a turbojet engine during Fluidic Thrust Vectoring (FTV) employed by injecting the secondary-jet at the throat of a convergent nozzle. The nozzle performance maps and effective nozzle throat area obtained from experiments are coupled with the performance of a conventional engine (without FTV) using an iterative algorithm developed as a part of this work. The performance is estimated for different flow rates of secondary-jet sourced either from a separate compressor or the engine's compressor. During FTV, the operating point shifted towards the surge line with increased turbine entry temperature. The desired and obtained vector angles and thrust magnitudes are different. At high secondary-jet flow rates, the turbine operation moved out of its performance map. These aspects should be incorporated while integrating the FTV at the system level, thus, asserting the importance of FTV studies coupled with engine performance.

Nomenclature

A	area (m ²)
A_{te}	effective nozzle throat area (m ²)
A_{ig}	geometric nozzle throat area (m ²)
C_o, C_1, C_2	constants
FTV	fluidic thrust vectoring
\dot{m}_f	mass flow rate of fuel (kg/s)
\dot{m}_i	mass flow rate of air at i^{th} station (kg/s)
$\dot{m}_{i,corr}$	corrected mass flow rate at i^{th} station (kg/s)
N	engine rotor speed (rpm)
NPR	nozzle pressure ratio
P	pressure (N/m ²)
PLA	pilot lever angle
R	gas constant (J/kg-K)
rpm	rotation per minute
T	temperature (K)
TET	turbine entry temperature (K)
\vec{T}	thrust vector ($T_{axial}\hat{I} + T_{yaw}\hat{J} + T_{pitch}\hat{K}$)
T_{axial}	thrust along the axial direction (N)
T_{pitch}	thrust along the pitch direction (N)
T_{yaw}	thrust along the yaw direction (N)
V	flow speed (m/s)
ΔA_{te}	change in the effective nozzle throat area (m ²)

This paper is a version of a presentation due to be given at the 2022 ISABE Conference

ρ	density (kg/m ³)
θ_y	vector angle (deg.)
γ	ratio of the specific heats
π_c	compressor pressure ratio

Subscripts

a	atmosphere/ambient
b or 3b	bleed
corr	corrected value
D	design condition
eng	engine
in	inlet
m	measured value
n	normalised value
oi	total condition at i^{th} station
r	relative
ref	reference value
s	secondary-jet
t	throat

Subscripts/Station Numbers

1	intake inlet/ambient
2	compressor inlet or intake exit
3	combustor inlet or compressor exit
4	turbine inlet or combustor exit
7	nozzle inlet
8	nozzle exit/throat

1.0 Introduction

Next-generation aircraft are characterised by higher range, loiter capability, less weight, volume, drag, noise, fuel burn and short take-off and landing (STOL) capabilities. Along with these, the aircraft is to be incorporated with a tailless planform to reduce drag [1]. Using engine thrust for pitch and yaw control by means of “Thrust Vectoring” is a suitable alternative for the tail (rudder and elevators). Thrust vectoring also helps carry out extreme manoeuvres and STOL capabilities, which would not be possible with conventional control surfaces owing to their aerodynamic limitations. Furthermore, the post-stall handling ability of an aircraft can be enhanced by incorporating thrust vectored flight control systems in an aircraft. Thrust vectored flight control enables an aircraft to stabilise beyond the limits posed by the external flow regime [2] and can be instrumental in preventing catastrophic failure [3]. For naval applications, implementing thrust vectored flight control can eliminate the need for catapult launchers and arresters on carrier ship decks. Lockheed Martin F-22 Raptor, Sukhoi Su-30MKI, Lockheed Martin F-35, Harrier Jump Jet are equipped with a mechanical thrust vectoring nozzle(s). In summary, thrust vectored flight control transfers the flight controls to the engine from conventional control surfaces, which helps overcome the limitations posed by conventional control surfaces.

Thrust vectoring is accomplished by deflecting the thrust away from the centreline, which leads to the generation of forces and moments in the yaw and pitch directions. Thrust vectoring can be broadly classified under two categories, mechanical thrust vectoring and fluidic thrust vectoring (FTV). Mechanical thrust vectoring can be employed by gimbaling the nozzle or introducing deflecting vanes/flaps to achieve vectoring of the exhaust jet [4]. Even though mechanical thrust vectoring is an effective approach to vectoring the jet, it requires integrating mechanical systems that can be complex and bulky, increasing the overall weight of the engine. On the contrary, FTV is simple to implement with a minimum weight

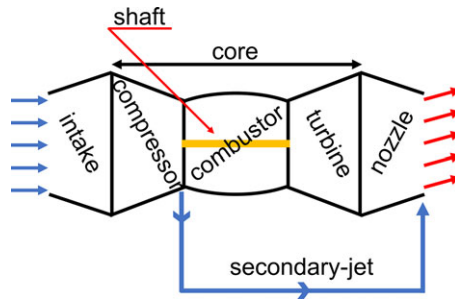


Figure 1. Components of a single-spool turbojet engine.

penalty since no additional moving parts are required. FTV employs a secondary stream (secondary-jet) in addition to the primary flow to create the desired effect of displacing the primary flow from its centre line. Prominent methods for FTV in subsonic and supersonic nozzles are co-flow, counter-flow, shock vectoring, throat skewing and subsonic skewing [1]. Yagle et al. [5] established that the throat skewing yielded higher gross thrust efficiency than other methods. The experimental study on a converging nozzle has shown that the secondary-jet injection at the nozzle exit deflects the thrust and forces the nozzle to operate at a reduced effective flow area [6]. The effect of the secondary-jet is maximum when the injection slot is at the exit [6]. These studies emphasised the flow dynamics during vectoring and evaluated the performance in terms of vector angle and thrust coefficient on a stand-alone nozzle. It is vital to acknowledge that in practice, the nozzle is attached to a gas turbine engine which is in turn fixed to the airframe. As reported by Lee and Lan [7], different optimal thrust deflection angles exist for the sustained maximum load factor, turn rate, and minimum turn radius. The earlier experimental studies [8, 9] on FTV showed that secondary-jet injection results in pressure rise at the nozzle inlet, which is expected to affect the engine operation. Additionally, the change in the effective flow area of the nozzle [6] may result in compressor surge or higher turbine entry temperature [10]. Thus, it is evident that using FTV will affect engine operation, moving it away from its initial operating point.

In an aircraft, the engine core (Fig. 1) is designed by the engine manufacturer, whereas the nozzle and intake are part of the airframe. Engine core, intake, and nozzle should work in harmony for optimum performance. The interaction between the components in the engine is analysed using their performance maps, which are a graphical representation of the corrected parameters (non-dimensional) governing the component operation [11]. The details of these component performance maps and how they are used for component matching are available in the open literature [9, 12]. The interaction between the components of a turbojet engine (Fig. 1) can be understood using thermodynamic cycle (Brayton cycle) analysis [13–15]. This exercise is termed ‘performance simulation of a gas turbine engine’ and can be carried out using commercially available software. The performance simulation includes two steps: design point calculation and off-design calculation. The design point calculation comprises the engine’s selection that involves selecting intake, compressor, combustor, turbine and nozzle. The off-design analysis includes estimating the engine performance at different operating conditions (including flight speed, altitude, and thrust level/engine rotor speed), i.e. evaluating the performance of the chosen components at different flight conditions. Commercially available simulation software are not capable of simulating engine performance during FTV operations since the nozzle performance maps for FTV [9] are not included. Thus, the effect of FTV on engine performance cannot be directly studied using existing performance simulation software. However, the software allows the user to change parameters related to the nozzle during off-design simulations. Using this feature and the performance maps for FTV [9], the performance of a jet engine could be estimated during FTV, and this forms the basis for the present work.

The objective of the present work is to estimate the performance of a single-spool turbojet engine during FTV. The novelty of the current work is the algorithm developed for coupling the experimental data from nozzle testing for FTV [9] and the commercially available performance simulation software,

Gasturb 13. The algorithm developed as a part of this work helps transfer the information from experiments on FTV capable nozzle to the performance simulation software, allowing estimation of engine performance during FTV. In the first part of this manuscript, the nozzle performance maps from the earlier experimental work [9] to implement FTV in the yaw direction in a convergent nozzle are discussed. In the second part of the manuscript, the basics associated with the performance/operation of a turbojet engine and modelling are discussed. In the third part of the manuscript, the coupling mechanism between the experimental data and the simulation software is discussed, followed by the algorithm adopted to study the performance of the engine during FTV. In the last section, the performance of the single-spool turbojet engine during FTV is discussed.

2.0 Nozzle performance maps for FTV

The performance maps for the nozzle with FTV using secondary-jet injection from the earlier experimental study [9] and their mathematical formulations required for simulations are discussed in this section.

For an FTV nozzle, three performance maps are required, namely (1) NPR-map, (2) T-map (Thrust-map) and (3) θ -map (vector angle map) [9]. The definitions of the parameters used in these maps are given by Equations (1)–(5) after incorporating modifications to the earlier definitions [9] to match the definitions used in the simulation software. These modifications are in terms of the reference conditions, thus only scaling the numerical values leaving the overall trend unaltered. The reference conditions are a temperature (T_{ref}) of 288.15K and pressure (P_{ref}) of 101,325Pa.

The corrected mass flow rate calculated at the inlet of the nozzle ($m_{7,\text{corr}}$) is given by Equation (1), where \dot{m}_7 is the mass flow rate, T_{07} is the stagnation temperature, P_{07} is the stagnation pressure at the nozzle inlet.

$$\text{Corrected mass flow rate at the nozzle inlet } (m_{7,\text{corr}}) = \frac{\dot{m}_7 \sqrt{T_{07}/T_{\text{ref}}}}{P_{07}/P_{\text{ref}}} \text{ kg/s} \quad (1)$$

The corrected mass flow rate of the secondary-jet ($m_{s,\text{corr}}$) at the exit of the secondary-jet injection slot is given by Equation (2), where \dot{m}_s is the mass flow rate, T_{os} is the stagnation temperature, P_{os} is the stagnation pressure of the secondary-jet.

$$\text{Corrected mass flow rate of secondary – jet } (m_{s,\text{corr}}) = \frac{\dot{m}_s \sqrt{T_{os}/T_{\text{ref}}}}{P_{os}/P_{\text{ref}}} \text{ kg/s} \quad (2)$$

The nozzle pressure ratio (NPR) is given by Equation (3), where P_{07} is the stagnation pressure at nozzle inlet and P_a is the atmospheric pressure.

$$\text{Nozzle Pressure Ratio (NPR)} = \frac{P_{07}}{P_a} \quad (3)$$

Normalised thrust is given by Equation (4), where $\vec{T}_m = T_{\text{axial}}\hat{\mathbf{I}} + T_{\text{yaw}}\hat{\mathbf{J}} + T_{\text{pitch}}\hat{\mathbf{K}}$ is obtained from the experiments, and $|\vec{T}_d|$ is the design value of the thrust magnitude (i.e. with Mach number equal to one at the throat).

$$\text{Normalised Thrust } (|\vec{T}_n|) = \frac{|\vec{T}_m|}{|\vec{T}_d|} \quad (4)$$

The yaw vector angle (θ_y) is given by Equation (5), where T_{yaw} is the yaw component and T_{axial} is the axial component of the thrust.

$$\text{Yaw vector angle } (\theta_y) = \tan^{-1} (T_{\text{yaw}}/T_{\text{axial}}) \quad (5)$$

The three performance maps are shown in Fig. 2(a) (NPR-map), (b) (T-map), and (c) (θ -map). For a given $m_{s,\text{corr}}$, the $|\vec{T}_n|$ varies quadratically with $m_{7,\text{corr}}$ (Fig. 2(b)), and the magnitude of θ_y varies linearly with $m_{7,\text{corr}}$ (Fig. 2(c)). Thus, for the given combination of $m_{s,\text{corr}}$ and $m_{7,\text{corr}}$, the thrust magnitude ($|\vec{T}_n|$) and vector angle (θ_y) can be determined using Equations (6) and (7), respectively, and the values of

Table 1. Values of coefficients in Equation (6) (T -map), Equation (7) (θ -map) and Equation (12) ($\% \Delta A_{te}$) for different $m_{s,corr}$

$m_{s,corr} (\times 10^{-3}) \text{kg/s}$	$ \vec{T}_n $ (T -map)			θ_y (θ -map)		$\% \Delta A_{te}$	
	C_2	C_1	C_0	C_1	C_0	C_1	C_0
0	75.428	-13.038	0.6817	0	0	0	0
2.71	78.428	-12.759	0.6478	-30.636	7.0309	141.88	-24.286
4.81	94.619	-15.302	0.7686	-71.075	16.272	189.09	-34.897
5.93	118.4	-19.932	1.0138	-83.09	19.537	231.95	-44.304
7.15	137.01	-22.617	1.1357	-89.738	21.732	263.78	-52.295

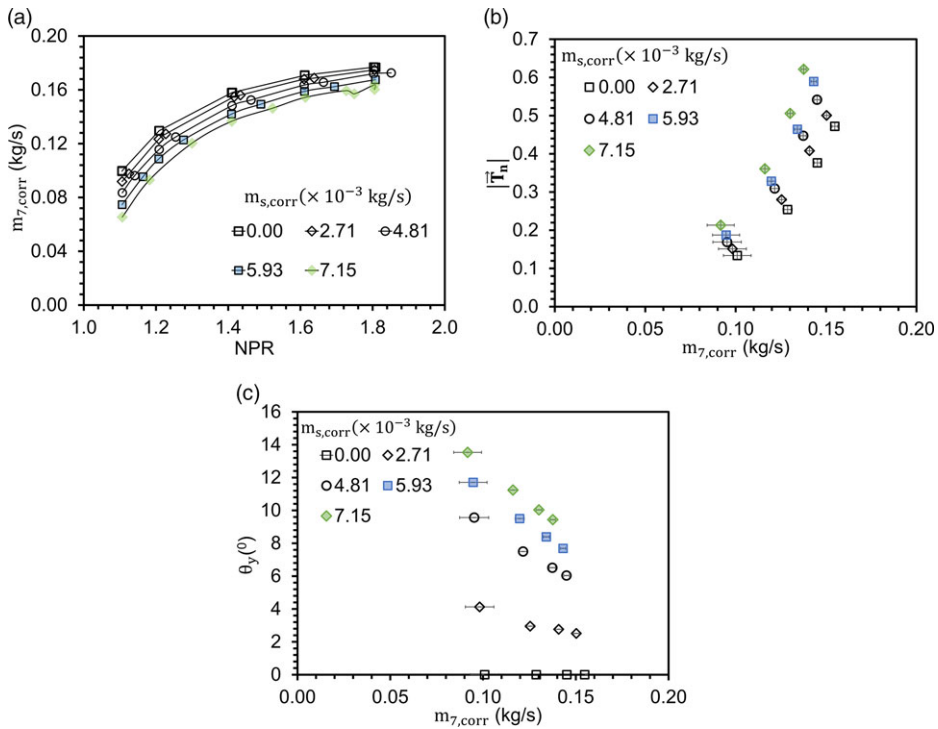


Figure 2. Nozzle performance maps (a) NPR-map, (b) T -map, and (c) θ -map for the nozzle.

the coefficients are given in Table 1. Equations (6) and (7) are used in the simulations for estimating θ_y and $|\vec{T}_n|$.

$$|\vec{T}_n| = C_2(m_{7,corr})^2 + C_1 \times m_{7,corr} + C_0, \text{ at } m_{s,corr} = \text{constant} \tag{6}$$

$$\theta_y = C_1 \times m_{7,corr} + C_0, \text{ at } m_{s,corr} = \text{constant} \tag{7}$$

The plots in NPR-map (Fig. 2(a)) shifts downwards with an increase in $m_{s,corr}$. Thus, at a given NPR, the $m_{7,corr}$ reduces due to the reduction in effective nozzle throat area [8, 11]. The magnitude of the effective nozzle area change ($\% \Delta A_{te}$) is computed using Equation (8), where A_{te} is effective throat area and A_{tg} is geometric throat area.

$$\% \text{ Change in the effective throat area } (\% \Delta A_{te}) = \left(\frac{A_{te} - A_{tg}}{A_{tg}} \right) \times 100 \tag{8}$$

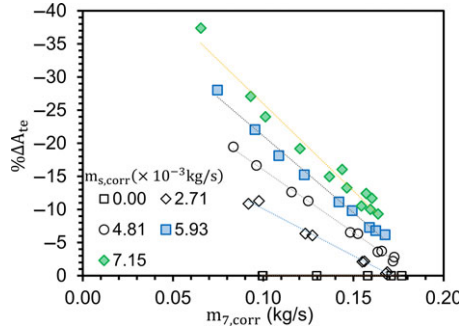


Figure 3. Nozzle throat area change ($\% \Delta A_{te}$) vs. $m_{7,corr}$ at different $m_{s,corr}$.

The effective throat area (A_{te}) is computed using Equation (9), where \dot{m}_7 is the mass flow rate, ρ_t is the flow density at the nozzle throat, and V_t is the flow speed at the nozzle throat, obtained from experiments.

$$\text{Effective Throat Area } (A_{te}) = \frac{\dot{m}_7}{\rho_t V_t} \tag{9}$$

Flow velocity at the nozzle throat (V_t) is computed using Equation (10) assuming isentropic flow, where P_{o7} is stagnation pressure at nozzle inlet, P_t is the static pressure at the nozzle throat, obtained from experiments. Nevertheless, the nozzle flow and secondary-jet interaction is an irreversible process associated with pressure loss. Since the secondary-jet is injected close to the nozzle exit, it is safe to assume that the flow remains isentropic up to the injection slot.

$$V_t = \sqrt{\frac{2\gamma RT_{o7}}{\gamma - 1} \left(1 - \left(\frac{P_{o7}}{P_t} \right)^{\frac{1-\gamma}{\gamma}} \right)} \tag{10}$$

The flow density at nozzle throat (ρ_t) is calculated using Equation (11), where P_t is the static pressure measured at the nozzle throat, and T_t is the static temperature at the nozzle throat estimated from the measured T_{o7} assuming isentropic flow.

$$\rho_t = \frac{P_t}{RT_t} \tag{11}$$

Figure 3 shows $\% \Delta A_{te}$ vs. $m_{7,corr}$ for different $m_{s,corr}$. The dashed line corresponding to each $m_{s,corr}$ shows the trend obtained by curve fitting using regression analysis. As observed from the plot, the values of $\% \Delta A_{te}$ are negative, indicating that the effective throat area (A_{te}) is less than the geometric throat area (A_{te}). For a given $m_{7,corr}$, the magnitude of $\% \Delta A_{te}$ increases with an increase in $m_{s,corr}$. Since $\% \Delta A_{te}$ is negative, it may be concluded that the effective throat area reduces with an increase in $m_{s,corr}$. The trend lines in the figure show a linear relationship between the $\% \Delta A_{te}$ and $m_{7,corr}$ at any given value of $m_{s,corr}$ and the slope depends on $m_{s,corr}$. Thus, the value of $\% \Delta A_{te}$ can be expressed as a function of $m_{s,corr}$ using Equation (12). The values of the constants in Equation (12) is given in Table 1.

$$\% \Delta A_{te} = C_1 \times m_{7,corr} + C_0 \tag{12}$$

3.0 Engine model and algorithm for FTV simulation

The elements of the engine modelling using the simulation software are discussed in the first part of this section, followed by the algorithm and the engine performance. The first part is intended to establish the connection between the experimental data and the simulation software, along with the rationale behind the algorithm developed for the analysis. Although Gasturb 13 [16] is used for simulations in this study, the procedure would remain the same for other commercially available software or in-house codes.

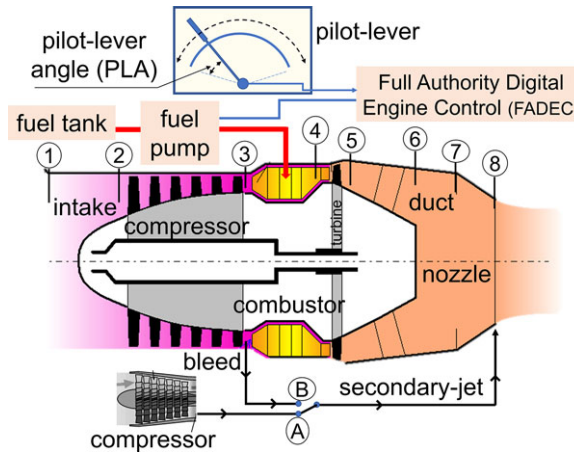


Figure 4. Schematic showing components and station numbers used.

3.1 Engine model

The performance of a single-spool turbojet engine can be evaluated by modelling its thermodynamic cycle [11] (Brayton cycle). The key performance parameters are thrust, thrust specific fuel consumption, surge margin, and turbine entry temperature (TET). The operational envelope of a turbojet engine is limited by the compressor surge margin and turbine entry temperature (TET). For a thrust vector enabled engine, the vector angle is added to the list of performance parameters. Among these performance parameters, thrust, vector angle, turbine entry temperature (TET) and surge margin are of interest in this study. A single spool turbojet jet engine chosen for current simulations is suitable for micro-air vehicle applications. However, the findings may be extended to the other gas turbines employing fluidic thrust vectoring.

The components of the single-spool turbojet engine chosen for the simulation and the station numbers are shown in Fig. 4. The single-spool turbojet engine comprises a single-stage compressor (between Station-2 and Station-3) mechanically connected to a single-stage turbine (between Station-4 and Station-5) via a shaft. The air to the compressor is supplied by an intake (between Station-1 and Station-2). A combustor (between Station-3 and Station-4) is placed between the compressor and turbine in which the aviation turbine fuel (Jet-A1) is combusted for energy addition. A convergent-type nozzle (between Station-7 and Station-8) with the throat at Station-8 is present at the exit of the turbine to convert the pressure energy to jet velocity producing thrust. The inter-component duct (between Station-5 and Station-7) connecting the turbine exit and the nozzle inlet is assumed to have no effect on the thermodynamic properties of the flow. The fuel is supplied into the combustion chamber by the fuel pump (Fig. 4). The fuel pump is operated by the FADEC (Full Authority Digital Engine Control) [17] based on the input from the pilot using ‘pilot-lever’. In an actual engine, the parameters, including the engine rotor speed, exhaust gas temperature, and compressor exit temperature, are monitored by the FADEC, and the fuel flow rate is controlled based on these parameters and the control input from the pilot. By changing the pilot lever, the thrust from the engine can be varied.

3.1.1 Modelling the nozzle used in experiments

The first stage of modelling comprises design point calculation, and the second stage comprises off-design calculations. The design point is modelled based on the shape and size of the nozzle used in experiments [9]. The nozzle shape is carried over as discharge coefficient, and the nozzle size is carried over as nozzle throat area. During the design point calculations, the discharge coefficient is an input parameter (among other parameters), and the nozzle throat area is an output parameter. Thus, during the design point calculations, the value of the discharge coefficient obtained from the experiments [9]

Table 2. Design point parameters of the turbojet engine chosen for simulation

Parameter	Value
Compressor pressure ratio	3.8
Combustion chamber pressure ratio	0.98
Compressor isentropic efficiency	0.73
Turbine isentropic efficiency	0.86
Combustor efficiency	0.95
Inlet mass flow rate	0.168kg/s
Nozzle thrust coefficient	0.97
Turbine Entry Temperature (TET)	1,178K
Altitude (above sea level)	0km
Flight Mach number	0
Net Thrust	0.095kN
Calorific value of the fuel (Jet A-1)	43.12MJ/kg
Design rotor speed (N_D)	96,500rpm
Nozzle discharge coefficient	0.95

*All other parameters were kept at their default values.

is given as an input, and the mass flow rate through the engine (another input parameter) was modified such that the geometric throat area of the nozzle estimated by the simulation software is equal to the nozzle throat area used in the experiments [9]. As a result of this, both the corrected mass flow rate at the nozzle inlet ($m_{7,corr}$) and the thrust magnitude from the simulations and experiments is equal.

The design point values of the engine used in this simulation are given in Table 2. For off-design simulations, the compressor and turbine maps available in Gasturb 13[®] are used for current simulations. Zero pressure loss in the intake is assumed ($P_{o2} = P_a$).

3.1.2 Sourcing the secondary-jet

Two options are considered for sourcing the secondary-jet required for vectoring, as shown in Fig. 4. The first option is to have an additional compressor different from the compressor in the jet engine, and the second option is to take the air from the compressor exit (station 3) of the core. The operation of this additional compressor is independent of the turbojet engine under study. A selector switch in the secondary-jet line is conceptualised for choosing the source, as indicated in Fig. 4. The secondary-jet line can be connected to either 'A' or 'B' based on the source of the secondary-jet. The practicality of the additional compressor (and the selector switch) is debatable and would depend on the engine and the final requirements. The secondary-jet sourcing concept may change for other engine categories (multi-spool turbojet and turbofan). Since the present study is aimed to study the effect of bleed on engine operation during FTV, the concept shown in Fig. 4 is considered.

3.1.3 Engine performance parameters

The compressor pressure ratio (π_c) is given by Equation (13) where P_{o3} is the total pressure at the compressor inlet, and P_{o2} is the total pressure at the compressor exit.

$$\text{Compressor pressure ratio } (\pi_c) = \frac{P_{o3}}{P_{o2}} \quad (13)$$

The corrected mass flow rate at compressor inlet ($m_{2,corr}$) is given by Equation (14), where \dot{m}_2 is the mass flow rate, P_{o2} is the total pressure, T_{o2} is the total temperature all at the compressor inlet.

$$\text{Corrected mass flow rate at the compressor inlet } (m_{2,corr}) = \frac{\dot{m}_2 \sqrt{T_{o2}/T_{ref}}}{P_{o2}/P_{ref}} \text{ kg/s} \quad (14)$$

The relative corrected rotor speed ($N_{\text{corr,r}}$) is given by Equation (15), where N is the rotor speed and T_{o2} is the total temperature at the compressor inlet during actual operation. N_D is the rotor speed, $T_{o2,D}$ is the total temperature at the compressor inlet at the design point, and T_{ref} is the reference value (288.15K).

$$\text{Relative corrected rotor speed } (N_{\text{corr,r}}) = \frac{N/\sqrt{T_{o2}/T_{\text{ref}}}}{N_D/\sqrt{T_{o2,D}/T_{\text{ref}}}} \quad (15)$$

The corrected mass flow rate of the bleed taken from the compressor exit is given by Equation (16) where \dot{m}_b is the mass flow rate of the bleed, P_{o3} is the total pressure at the compressor exit, T_{o3} is the total temperature at the compressor exit.

$$\text{Corrected mass flow rate of bleed } (m_{3b,\text{corr}}) = \frac{\dot{m}_b \sqrt{T_{o3}/T_{\text{ref}}}}{P_{o3}/P_{\text{ref}}} \text{ kg/s} \quad (16)$$

3.2 Algorithm for incorporating FTV in the simulation software

Employing FTV is considered under the off-design operation of the jet engine. During off-design operation, the nozzle throat area (A_8), nozzle thrust coefficient, and discharge coefficient can be varied. As observed earlier in Fig. 3, secondary-jet injection reduces the effective nozzle throat area (A_{te}). Thus, the FTV can be simulated as the nozzle throat area at station-8 (A_8) in off-design simulations. Based on the flow rate through the nozzle and the secondary-jet, the nozzle throat area change ($\% \Delta A_{te}$) can be estimated from Equation (12). This change in the throat area ($\% \Delta A_{te}$) is given as a change in the nozzle area at station-8 ($\% \Delta A_8$) in the off-design simulations. For example, if $m_{7,\text{corr}} = 0.154$ and $m_{s,\text{corr}} = 2.71 \times 10^{-3}$, then a throat area change ($\% \Delta A_8$) equal to -2.56% is entered into the simulation software, and the new operating point is calculated. This new operating point has $m_{7,\text{corr}}$ different from 0.154. Thus, the $\% \Delta A_{te}$ at this new operating point would be different from -2.56% and the new $\% \Delta A_{te}$ is considered. The procedure is repeated until the area changes converge. The algorithm is best described using the flow chart in Fig. 5(a). To minimise complexities, all the simulations are carried out assuming steady-state operation. Thus, a change in the throat area of the nozzle instantly drives the engine to a new operating point without considering transient operations, i.e. the inertia effects are ignored (both thermodynamic and mechanical). It is vital to note that the final operating point predicted both with and without considering the inertial effects would be the same, but the path taken would be different. Since the objective is to understand the effect on the steady-state operation, satisfactory results would be obtained using this algorithm.

Consider the engine operating at a relative corrected rotor speed of $(N_{\text{corr,r}})_{\text{start}}$, at which the corrected mass flow rate at the nozzle inlet (station 7) is given by $(m_{7,\text{corr}})_{\text{start}}$. This operating condition is termed as ‘starting-point’. Step 1, the secondary-jet with $m_{s,\text{corr}}$ is activated and is maintained constant for all the subsequent steps. Step 2, the change in the nozzle throat area $(\% \Delta A_{te})_{\text{step2}}$ is estimated using Equation (12) corresponding to the chosen $(m_{7,\text{corr}})_{\text{start}}$ and $m_{s,\text{corr}}$. Step 3, the value of $(\% \Delta A_{te})_{\text{step2}}$ is input to the software (off-design operation), yielding a new operating point for the engine, and value of $(m_{7,\text{corr}})_{\text{step3}}$ is computed. Step 4, using the values of $(m_{7,\text{corr}})_{\text{step3}}$ and $m_{s,\text{corr}}$, the new nozzle throat area change $(\% \Delta A_{te})_{\text{step4}}$ is calculated using Equation (12). Step 5, the value $|(\% \Delta A_{te})_{\text{step2}} - (\% \Delta A_{te})_{\text{step4}}|$ is computed, and if it is within the chosen tolerance limit, the computations are stopped. Otherwise, the $(m_{7,\text{corr}})_{\text{step3}}$ is given as input to step 2, and steps 2 to 5 are repeated until the convergence criterion is satisfied at step 5. After the convergence criterion is met, the new operating point at step 3 is the final equilibrium operating point of the jet engine after the secondary-jet injection.

The algorithm is demonstrated in Fig. 5(b) using the case of $(m_{7,\text{corr}})_{\text{start}} = 0.155$ and $m_{s,\text{corr}} = 2.71 \times 10^{-3}$. The open diamonds show the value of $(m_{7,\text{corr}})_{\text{step3}}$ during each iteration and open squares show the value of $|(\% \Delta A_{te})_{\text{step2}} - (\% \Delta A_{te})_{\text{step4}}|$ during each iteration. Iteration number zero corresponds to the starting point in the algorithm, and iteration number 7 corresponds to the new operating point. As observed from the plot, the quantity $|(\% \Delta A_{te})_{\text{step2}} - (\% \Delta A_{te})_{\text{step4}}|$ decreases with each iteration

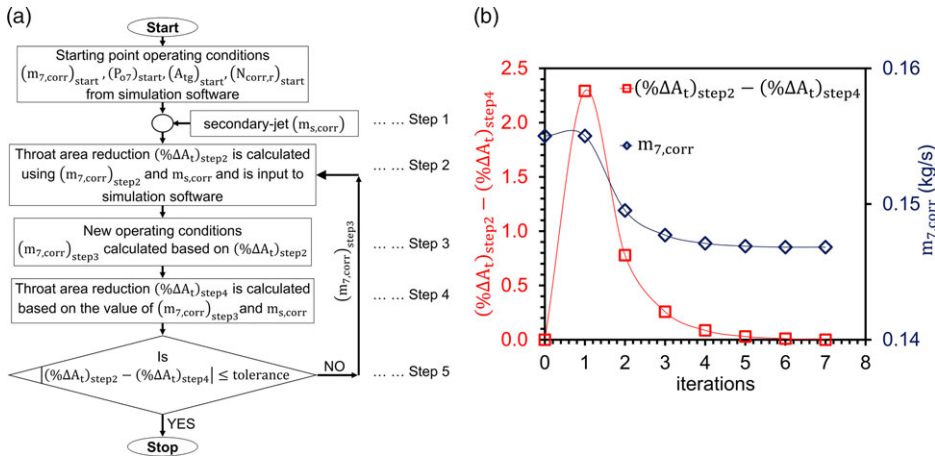


Figure 5. Algorithm for estimating the response of the engine during fluidic thrust vectoring, (a) flow chart, (b) convergence with the iteration number.

and reaches convergence. The value of $m_{7,corr}$ at new operating point is different from that of the starting point. Similarly, other parameters at the new operating point are different from the starting point. In step 3, if the operating point crosses the surge line leading to instability, the algorithm is terminated, and the case is termed ‘Not-Converged’. It may be concluded that the FTV may not be implemented for these combinations of $m_{7,corr}$ and $m_{s,corr}$.

4.0 Engine performance during FTV

The engine performance without FTV is considered in the first part of this section, followed by the performance with FTV. The results of the first part would help explain the performance during FTV.

4.1 Engine performance without FTV (conventional engine)

The thrust from the engine is varied by changing the fuel flow rate using the pilot-lever (Fig. 4). The relative corrected value of the rotor speed ($N_{corr,r}$) at different fuel flow rates (\dot{m}_f) is shown in Fig. 6(a), and normalised thrust ($|\vec{T}_{n,eng}|$) vs. fuel flow rate (\dot{m}_f) is shown in Fig. 6(b). The fuel flow rate is reduced by decreasing the pilot lever angle (PLA) and vice-versa. Both the figures show plots corresponding to different values of $m_{3b,corr}$. The case with no bleed extraction ($m_{3b,corr} = 0$) is discussed first, followed by other cases. As observed in the plots, both the rotor speed and thrust increases with an increase in the fuel flow rate. The rate of change of $N_{corr,r}$ with \dot{m}_f is large for $1.5 \times 10^{-3} < \dot{m}_f < 2 \times 10^{-3}$ compared to $\dot{m}_f > 2 \times 10^{-3}$ kg/s (Fig. 6(a)). The rate of change of $|\vec{T}_{n,eng}|$ with \dot{m}_f is large for $1.5 \times 10^{-3} < \dot{m}_f < 2 \times 10^{-3}$ compared to $\dot{m}_f > 2 \times 10^{-3}$ kg/s (Fig. 6(b)). The energy added is directly proportional to the fuel flow rate, thus, the energy available to the turbine is directly proportional to the amount of fuel added per second. The excess energy available to the turbine accelerates the rotor speed to a higher value which increases the mass flow rate and compressor pressure ratio (Fig. 7). At any given fuel flow rate, with the bleed from the exit of the compressor ($m_{3b,corr} > 0$), the rotor speed reduces, and the magnitude of this decrement increases with an increase in $m_{3b,corr}$.

The performance is better understood by plotting the engine operating points on the compressor map shown in Fig. 7. The inserts in the figure show the zoomed-in view of the plots for better visibility of the data points. For a conventional engine, the operating points on the compressor map correspond to the throttle change. The operating line for different $m_{3b,corr}$ is shown in Fig. 7. For $m_{3b,corr} = 0$, with an increase in throttle, the rotor speed, mass flow rate, and compressor pressure ratio increase leading to

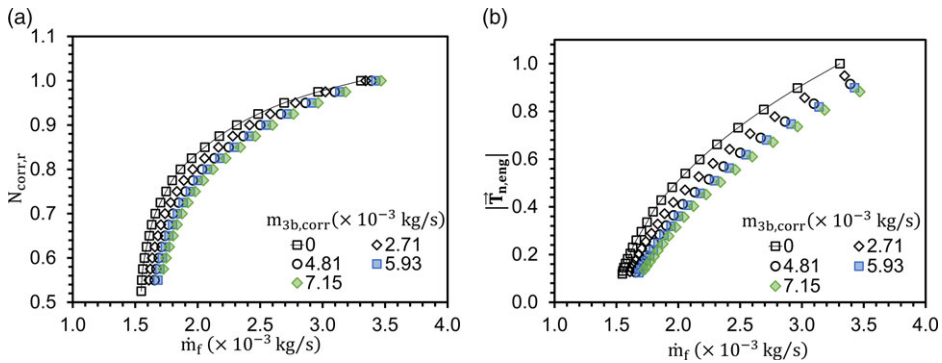


Figure 6. (a) Relative corrected speed ($N_{corr,r}$) vs. fuel flow rate (\dot{m}_f), (b) Normalised thrust from the engine ($|\vec{T}_{n,eng}|$) vs. fuel flow rate (\dot{m}_f), for different bleeds ($m_{3b,corr}$) at compressor exit.

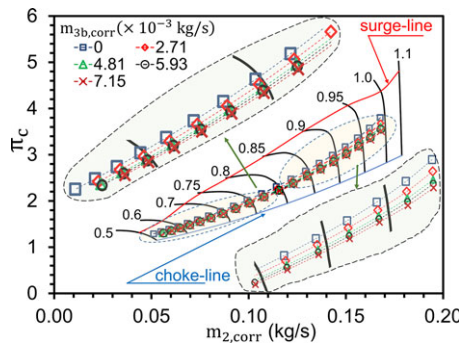


Figure 7. Compressor map showing the engine operating points during engine operation without ($m_{3b,corr} = 0$) and with bleed ($m_{3b,corr} > 0$).

an increase in the thrust as observed earlier in Fig. 6. With the extraction of bleed at the compressor exit ($m_{3b,corr} > 0$), the operating line shifts towards the choke-line. Thus, the compressor pressure reduces with the extraction of the bleed from the compressor exit. The extraction of air at the compressor exit would reduce the mass flow rate available for the turbine. Hence, the work available for the compressor would reduce, leading to a decrement in the rotor speed. This reduction in rotor speed would cause a decrement in the compressor pressure ratio. The reduction in the pressure ratio combined with a reduction in the mass flow rate through the nozzle leads to thrust decrement, as observed earlier in Fig. 6(b).

In summary, the reduction (or increment) in the fuel flow rate decreases (or increases) the compressor pressure ratio, rotor speed, and thrust. At a given fuel flow rate, the extraction of the bleed at the compressor exit causes a reduction in the compressor pressure ratio, rotor speed and thrust.

4.2 Engine performance during FTV

The objective is to achieve a vector angle (θ_y) of 2.3° , 6.7° , and 7.9° . At $N_{corr,r} = 0.83$, the vector angles can be achieved by injecting secondary-jet with $m_{s,corr}$ of 2.71×10^{-3} , 5.93×10^{-3} , and 7.15×10^{-3} , respectively, obtained from Equation (7) (Fig. 2).

The engine performance during FTV is evaluated for two configurations. In the first configuration, the secondary-jet required for FTV is assumed to be taken from an additional compressor different from the compressor of the turbojet engine chosen for simulation. In the second configuration, the secondary-jet is taken as the bleed from the compressor exit (station 3). The engine response is evaluated by observing the operating point on the compressor map, the thrust magnitude, and the vector angle. During the

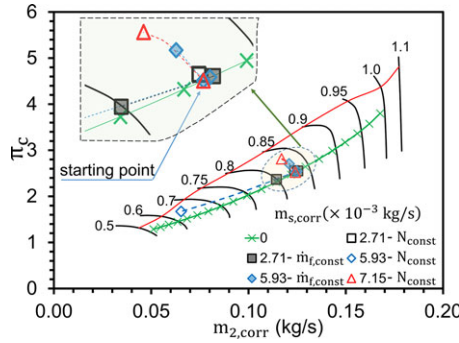


Figure 8. Compressor performance map showing operating points during FTV without bleed.

injection of the secondary-jet, the fuel flow rate can be varied or maintained constant. Hence, two sets of simulations were carried out for each configuration. In the first set of simulations, the fuel flow rate is held constant, termed ‘ $\dot{m}_{f, \text{const}}$ ’, and in the second set of simulations, the fuel flow rate is varied such that the engine rotor speed is kept constant, termed ‘ N_{const} ’.

4.2.1. Without bleed from the compressor

In this configuration, the secondary-jet required for FTV is assumed to be taken from an additional compressor different from the compressor of the turbojet engine. Thus, the bleed option is switched off all through the simulations.

Figure 8 shows the operating points on the compressor map for different $m_{s, \text{corr}}$. The green stars correspond to the operation with a change in throttle (PLA) and no secondary-jet injection ($m_{s, \text{corr}} = 0$). The open squares correspond to FTV with $m_{s, \text{corr}} = 2.71 \times 10^{-3}$ and N_{const} . The filled squares correspond to FTV with $m_{s, \text{corr}} = 2.71 \times 10^{-3}$ and $\dot{m}_{f, \text{const}}$. The open diamonds correspond to FTV with $m_{s, \text{corr}} = 5.93 \times 10^{-3}$ and N_{const} . The filled diamonds correspond to FTV with $m_{s, \text{corr}} = 5.93 \times 10^{-3}$ and $\dot{m}_{f, \text{const}}$. The open triangles correspond to FTV with $m_{s, \text{corr}} = 7.15 \times 10^{-3}$ and N_{const} . The case with constant fuel flow rate ($\dot{m}_{f, \text{const}}$) is discussed first, followed by N_{const} . Before the secondary-jet injection, the operating point is indicated as the ‘starting point’ in the figure. As observed in Fig. 8, after the secondary-jet injection, the operating point shifts to a lower rotor speed resulting in reduced mass flow rate and pressure ratio. This reduction in rotor speed is not due to the decrease in PLA observed earlier in Fig. 6.

For a converging nozzle assuming isentropic flow, the mass flow rate is given by Equation (17) where P_{07} in the stagnation pressure at the nozzle inlet, T_{07} is the stagnation temperature at the nozzle inlet, P_a is ambient pressure and A_8 is the nozzle throat area. From Equation (17), the mass flow rate through the nozzle is directly proportional to the nozzle throat area and has a non-linear relationship with the upstream pressure. During FTV, the change in the effective throat area dominates compared to the change in the pressure at the nozzle inlet, thus, reducing the mass flow rate and shifting the operating point to the left. This reduction in the mass flow rate reduces the power available for the turbine reducing the rotor speed and π_c . The overall effect is that the operating point moves closer to the surge line. Thus, compared to a conventional engine, the engine with FTV should have a higher surge margin.

$$\dot{m}_8 = P_a A_8 \sqrt{\frac{2\gamma}{RT_{07}(\gamma - 1)}} \sqrt{\left(\frac{P_{07}}{P_a}\right)^{\frac{\gamma-1}{\gamma}} \left\{ \left(\frac{P_{07}}{P_a}\right)^{\frac{\gamma-1}{\gamma}} - 1 \right\}} \tag{17}$$

For $m_{s, \text{corr}} = 2.71 \times 10^{-3}$, the operating point shifts to $N_{\text{corr}, r} = 0.8$, and for $m_{s, \text{corr}} = 5.93 \times 10^{-3}$, the operating point shifts to $N_{\text{corr}, r} = 0.62$. For $m_{s, \text{corr}} = 7.15 \times 10^{-3}$, the operating point moved out of the turbine map (operational envelope), and the algorithm did not converge, which is the case of the ‘Not-Converged’ algorithm mentioned in the previous section. It is asserted that, after the injection of the

Table 3. Vector angle (θ_y) and normalised thrust ($|\vec{T}_n|$) at different secondary-jet ($m_{s,corr}$) without bleed

$m_{s,corr} (\times 10^{-3})$ kg/s	$\dot{m}_{f,const}$				N_{const}			
	$\theta_y(^{\circ})$		$ \vec{T}_n $		$\theta_y(^{\circ})$		$ \vec{T}_n $	
	Desired	Obtained	Initial	Final	Desired	Obtained	Initial	Final
2.71	2.3	2.53	0.47	0.47	2.3	2.35	0.47	0.53
5.93	6.7	10.62	0.47	0.24	6.7	7.28	0.47	0.65
7.15	Not-Converged				7.9	8.95	0.47	0.69

Table 4. Turbine entry temperature (TET) during FTV at different $m_{s,corr}$ without bleed

$m_{s,corr} (\times 10^{-3})$ kg/s	$\dot{m}_{f,const}$		N_{const}	
	Initial	Final	Initial	Final
2.71	952.4K	981.7K	952.4K	990.6K
5.93	952.4K	1254.9K	952.4K	1146.6K
7.15	Not-Converged		952.4K	1308.1K

secondary-jet with $m_{s,corr} = 7.15 \times 10^{-3}$ due to the higher magnitude of reduction in the mass flow rate, the turbine is not able to meet the power required for the compressor leading to unstable operation. At this juncture, it may be concluded that there is an upper limit on the amount of secondary-jet injected into the nozzle for FTV operations for the safe operation of the engine. Now consider the case with N_{const} . For this, the FADEC modifies the fuel flow rate such that the rotor speed is maintained constant. As observed from Fig. 8, during FTV, the operating point shifts towards the surge line on the same speed line, the compressor pressure ratio increases, and the mass flow rate reduces. For $m_{s,corr} = 2.71 \times 10^{-3}$, the operating point is closer to the starting point and for $m_{s,corr} = 5.93 \times 10^{-3}$ and 7.15×10^{-3} , the operating point moves closer to the surge line. Thus, with an increase in $m_{s,corr}$ the operating point would shift closer to the surge line reducing the surge margin, which is similar to $\dot{m}_{f,const}$ case. At this juncture, it may be concluded that the compressor operation shifts towards the surge line during FTV operations. In contrast to $\dot{m}_{f,const}$, the algorithm converged for $m_{s,corr} = 7.15 \times 10^{-3}$ with N_{const} due to the addition of higher energy to the gas by increasing the fuel flow rate. The increment in the fuel flow rate enables the turbine to extract more energy sustaining the engine operation, however, with higher turbine entry temperature (Table 4). Thus, it may be concluded that during FTV, in addition to controlling the flow rate of the secondary-jet, the flow rate of the fuel should also be varied.

The vector angles (θ_y), thrust magnitudes ($|\vec{T}_n|$) for all the cases are given in Table 3, and turbine entry temperature (TET) is given in Table 4. At the start of this section, the goal was set to achieve three different vector angles (θ_y) given as ‘desired’ values in Table 3, and the values obtained from simulations are given as ‘obtained’ values. The initial (before FTV) and final (after FTV) values of the normalised thrust ($|\vec{T}_n|$) are given in Table 3. As observed in the table, for both $\dot{m}_{f,const}$ and N_{const} , the values of θ_y obtained during FTV is higher compared to the desired values. The final magnitude of $|\vec{T}_n|$ during FTV is lower compared to the initial value for $\dot{m}_{f,const}$, whereas, the final magnitude is higher for N_{const} . For both $\dot{m}_{f,const}$ and N_{const} , the difference between the initial (desired) and final (obtained) values increase with an increase in $m_{s,corr}$. The difference between the desired value (initial) and the obtained (final) value is due to a reduction in the magnitude of $m_{7,corr}$ after the secondary-jet injection. Thus, the actual magnitude of the $m_{s,corr}$ required to achieve a specified vector angle is different from the values estimated from Fig. 2. The actual value of $m_{s,corr}$ can be estimated only by the coupled analysis involving the engine performance with FTV. Another parameter concerning engine safety is the turbine entry temperature (TET). The initial (before FTV) and final (after FTV) values of TET are shown in Table 4. From the

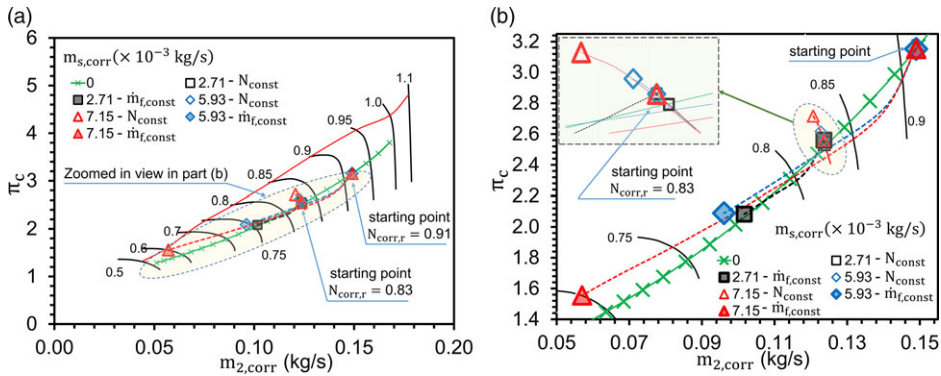


Figure 9. Compressor performance map showing (a) all operating points (b) zoomed-in view during FTV with bleed.

table, it may be concluded that the TET is higher during FTV. For $\dot{m}_{f,const}$, the increase in the fuel-air ratio is the cause for the rise in TET, whereas for N_{const} the increase in the fuel flow is the cause for the rise in TET.

This set of simulations demonstrates the importance of the coupled analysis involving the engine performance while evaluating the implementation of the FTV. The initial and final values of $|\vec{T}_n|$ and the obtained values of θ_y can be used to develop the control law for implementing FTV.

3.2.2 With bleed from the compressor

In this configuration, the secondary-jet required for FTV is assumed to be taken from the compressor exit (station 3) of the turbojet engine. Thus, the bleed option is switched on all through the simulations. Since the secondary-jet required for the vectoring is taken from the compressor exit (station 3), $m_{3b,corr} = m_{s,corr}$. Similar to the previous case, two sets of simulations were carried out, one with “ $\dot{m}_{f,const}$ ” and the other with “ N_{const} ”.

Figure 9(a) shows operating points on the compressor map during FTV with bleed at the compressor exit, and Fig. 9(b) show the zoomed-in view of the same points. Two starting points are indicated, one at $N_{corr,r} = 0.83$ and the other at $N_{corr,r} = 0.91$. At $N_{corr,r} = 0.83$, the simulations did not converge for $m_{s,corr} = 5.93 \times 10^{-3}$ and $m_{s,corr} = 7.15 \times 10^{-3}$ with $\dot{m}_{f,const}$. Thus, the speed was increased to $N_{corr,r} = 0.91$, and the simulations for $m_{s,corr} = 5.93 \times 10^{-3}$ and $m_{s,corr} = 7.15 \times 10^{-3}$ were repeated with $\dot{m}_{f,const}$. The green stars correspond to the operation with the throttle change (PLA) with no secondary-jet injection and no bleed. The open squares correspond to FTV with $m_{s,corr} = 2.71 \times 10^{-3}$ and N_{const} . The filled squares correspond to FTV with $m_{s,corr} = 2.71 \times 10^{-3}$ and $\dot{m}_{f,const}$. The open diamonds correspond to FTV with $m_{s,corr} = 5.93 \times 10^{-3}$, and N_{const} . The open triangles correspond to FTV with $m_{s,corr} = 7.15 \times 10^{-3}$, and N_{const} . The filled diamonds correspond to FTV with $m_{s,corr} = 5.93 \times 10^{-3}$ and $\dot{m}_{f,const}$. The filled triangles correspond to FTV with $m_{s,corr} = 7.15 \times 10^{-3}$ and $\dot{m}_{f,const}$. The starting point for filled diamond and filled square is at $N_{corr,r} = 0.91$. As observed from Fig. 9(a) or Fig. 9(b), the operating point shifts closer to surge-line during FTV, and the magnitude of shift increases with an increase in the $m_{s,corr}$. This behaviour is similar to the configuration with no-bleed. However, the magnitude of the shift in the operating point during FTV with bleed is less compared to the case without bleed. The simulations did not converge for $m_{s,corr} = 5.93 \times 10^{-3}$ and 7.15×10^{-3} with $\dot{m}_{f,const}$. For $m_{s,corr} = 7.15 \times 10^{-3}$, the simulations did not converge for the case with no-bleed, whereas, for $m_{s,corr} = 5.93 \times 10^{-3}$, the algorithm converged for the case without bleed, and it did not converge for the case with bleed. This is due to the reduction in the mass flow rate into the turbine after the bleed is extracted at the compressor exit. The reduced mass flow rate flowing through the turbine leads to a decrease in the power available for the compressor, due to which rotor speed decreases continuously, resulting in engine shutdown. After the starting point was moved to $N_{corr,r} = 0.91$, the mass flow rate through the compressor increases. This additional mass flow

Table 5. Vector angle (θ_y) and normalised thrust ($|\vec{T}_n|$) at different secondary-jet ($m_{s,corr}$) with bleed

$m_{s,corr} (\times 10^{-3}) \text{kg/s}$	$\dot{m}_{f,const}$				N_{const}			
	$\theta_y(^{\circ})$		$ \vec{T}_n $		$\theta_y(^{\circ})$		$ \vec{T}_n $	
	Desired	Obtained	Initial	Final	Desired	Obtained	Initial	Final
2.71	2.3	2.86	0.46	0.37	2.3	2.38	0.46	0.52
5.93	Not-Converged				6.7	7.47	0.46	0.62
7.15	Not-Converged				7.9	9.15	0.46	0.66

Table 6. Vector angle (θ_y) and normalised thrust ($|\vec{T}_n|$) at different secondary-jet ($m_{s,corr}$) with bleed

$m_{s,corr} (\times 10^{-3}) \text{kg/s}$	$\dot{m}_{f,const}$			
	$\theta_y(^{\circ})$		$ \vec{T}_n $	
	Desired	Obtained	Initial	Final
5.93	6.2	8.89	0.61	0.23
7.15	7.5	13.16	0.61	0.40

Table 7. Turbine entry temperature (TET) during FTV at different $m_{s,corr}$ with bleed

$m_{s,corr} (\times 10^{-3}) \text{kg/s}$	Starting point at $N_{corr,r} = 0.83$				Starting point at $N_{corr,r} = 0.91$	
	$\dot{m}_{f,const}$		N_{const}		$\dot{m}_{f,const}$	
	Initial	Final	Initial	Final	Initial	Final
2.71	952.4K	1037.0K	952.4K	1040.5K	–	–
5.93	Not-Converged		952.4K	1284.9K	1031.7K	1292.8K
7.15	Not-Converged		952.4K	1499.6K	1031.7K	1828.0K

rate allows extracting the higher bleed flow of 5.93×10^{-3} and 7.15×10^{-3} and sufficient mass flow of air is available to the turbine for the successful operation of the engine. Thus, it appears that the bleed extraction may not be suitable for all the operating conditions and may require an additional compressor. This observation further strengthens the earlier finding that the strategy to be adopted for implementing FTV would depend on the operational requirements.

The vector angle (θ_y) and normalised thrust ($|\vec{T}_n|$) with the bleed is given in Table 5 for the cases with starting point at $N_{corr,r} = 0.83$, and in Table 6 for the cases with starting point at $N_{corr,r} = 0.91$. Similar to the previous case with no-bleed, the vector angle obtained is higher than the desired value for all the cases. The difference in the magnitudes of desired and obtained value increases with an increase in $m_{s,corr}$. For the case with $m_{s,corr} = 7.15 \times 10^{-3}$, the obtained value is twice the desired value (Table 7). The final $|\vec{T}_n|$ is lower than the initial value for $\dot{m}_{f,const}$, and final $|\vec{T}_n|$ is higher than the initial value for N_{const} . The magnitude of increase in the thrust for the N_{const} case is small compared to the magnitude of reduction in the thrust for $\dot{m}_{f,const}$.

The turbine entry temperatures (TETs) for different test cases are shown in Table 7. The values under the column ‘Initial’ correspond to the starting point, and the column ‘Final’ correspond to the TET during FTV. In both the tables, it is clear that the TET during FTV is higher than the value before FTV. From Tables 4 and 7, it is clear that during FTV operation, the TET increases. Thus, for implementing

FTV, the turbine should handle higher flow temperatures. The recent success of implementing ceramic matrix composites [18] in gas turbines would enable FTV in future aircraft.

4.0 Conclusion

The nozzle performance maps obtained from earlier experiments conducted on a stand-alone converging nozzle to implement FTV using the secondary-jet injection technique are discussed. From these maps, the mathematical relations necessary for the simulations are obtained. The NPR-map resembles the nozzle operation with a reduced throat area, and the magnitude of the change in the effective flow area was estimated from the experimental data. For a given $m_{s,corr}$, the magnitude of the change in the effective throat area ($\% \Delta A_{te}$) was found to decrease linearly with $m_{7,corr}$. This $\% \Delta A_{te}$ is used in performance simulation software (Gasturb 13) using the algorithm developed to study the performance of a single spool turbojet engine during FTV.

Based on the vector angle required, the magnitude of $m_{s,corr}$ is chosen, and corresponding the area reduction (from experimental data) is given as input to the simulation software using the algorithm developed in this work. In the simulations, two configurations were considered based on the source of the secondary-jet. In the first configuration, the secondary-jet is sourced from an additional compressor different from the compressor in the turbojet engine. In the second configuration, the secondary-jet is taken from the compressor exit of the turbojet engine, termed 'bleed extraction'. In each of the configurations, two sets of simulations were carried out, one while maintaining the throttle constant ($\dot{m}_{f,const}$) and the other maintaining the rotor speed constant (N_{const}).

During FTV, for both the configurations, the engine operation was found to shift towards the surge line, reducing the available surge margin with $\dot{m}_{f,const}$ and N_{const} . The TET was found to be higher during FTV for both the configurations and with $\dot{m}_{f,const}$ and N_{const} . Thus, compared to a conventional engine, the engine with FTV should have a higher surge margin and should be able to handle higher TET. For $\dot{m}_{f,const}$, the final magnitude of $|\vec{T}_n|$ is lower compared to the initial value whereas, for N_{const} the final magnitude of $|\vec{T}_n|$ is higher compared to the initial value. Based on the demand from the flight controls, one of the two ($\dot{m}_{f,const}$ or N_{const}) strategies or a combination of them may be adopted. For both the configurations, the values of θ_y obtained during FTV is higher compared to the desired values with $\dot{m}_{f,const}$ and N_{const} . Thus, the magnitude of $m_{s,corr}$ required is different from that expected from the experiments on a stand-alone nozzle. For some test conditions ($m_{s,corr} = 7.15 \times 10^{-3}$ and without bleed and $\dot{m}_{f,const}$) the turbine operation moves out of its performance map, suggesting that the FTV that can be achieved may be limited based on the engine characteristics. This demonstrates that for evaluating the performance of FTV for an aircraft, the analysis on a stand-alone nozzle is insufficient and should include the coupled analysis.

References

- [1] Miller, D.N. and Flamm, J.D. Air-breathing propulsion flowpath applications, fundamentals and applications of modern flow control, American Institute of Aeronautics and Astronautics, Reston, VA, pp. 373–402, 2009. DOI: [10.2514/5.9781563479892.0373.0402](https://doi.org/10.2514/5.9781563479892.0373.0402)
- [2] Gal-Or, B. Safe jet aircraft, *Int J Turbo Jet Engines*, 1994, **11**, (1), pp 1–10. DOI: [10.1515/TJJ.1994.11.1.1](https://doi.org/10.1515/TJJ.1994.11.1.1)
- [3] Gal-Or, B., Sherbaum, V. and Lichtsinder, M. Fundamentals of catastrophic failure prevention by thrust vectoring, *J Aircr*, 1995, **32**, (3), pp 577–582. DOI: [10.2514/3.46758](https://doi.org/10.2514/3.46758)
- [4] Gal-Or, B. Fundamental concepts of vectored propulsion, *J Propuls Power*, 1990, **6**, (6), pp 747–757. DOI: [10.2514/3.23281](https://doi.org/10.2514/3.23281)
- [5] Yagle, P.J., Miller, D.N., Ginn, K.B. and Hamstra, J.W. Demonstration of fluidic throat skewing for thrust vectoring in structurally fixed nozzles, *J Eng Gas Turbines Power*, 2001, **123**, (3), pp 502–507. DOI: [10.1115/1.1361109](https://doi.org/10.1115/1.1361109)
- [6] Mcardle, J.G. Internal characteristics and performance of an aerodynamically controlled, variable-discharge convergent nozzle, NACA-TN-4312, 1958.
- [7] Lee, P.-H. and Lan, C.E. Effect of thrust vectoring on level-turn performance, *J Aircr*, 1992, **29**, (3), pp 509–511. DOI: [10.2514/3.46191](https://doi.org/10.2514/3.46191)
- [8] Sekar, T.C., Kushari, A., Mody, B. and Uthup, B. Fluidic thrust vectoring using transverse jet injection in a converging nozzle with aft-deck, *Exp Therm Fluid Sci*, 2017, **86**, pp 189–203. DOI: [10.1016/j.expthermflusci.2017.04.017](https://doi.org/10.1016/j.expthermflusci.2017.04.017)

- [9] Sekar, T.C., Jaiswal, K., Arora, R., Sundararaj, R.H., Kushari, A. and Acharya, A. Nozzle performance maps for fluidic thrust vectoring, *J Propuls Power*, 2021, **37**, (2), pp 314–325. DOI: [10.2514/1.B38044](https://doi.org/10.2514/1.B38044)
- [10] Sundararaj, R.H., Sekar, T.C., Arora, R., Rao, A.N. and Kushari, A. “Performance simulation of an engine retrofitted with thrust vectoring capabilities,” *Volume 2: Combustion, Fuels, and Emissions; Renewable Energy: Solar and Wind; Inlets and Exhausts; Emerging Technologies: Hybrid Electric Propulsion and Alternate Power Generation; GT Operation and Maintenance; Materials and Manufacturing (Including Coatings, Composites, CMCs, Additive Manufacturing); Analytics and Digital Solutions for Gas Turbines/Rotating Machinery, Chennai, Tamil Nadu, India*. 5–6 December 2019. ASME. DOI: [10.1115/GTINDIA2019-2448](https://doi.org/10.1115/GTINDIA2019-2448)
- [11] Cohen, H., Rogers, G.F.C. and Saravanamuttoo, H.I.H., *Gas Turbine Theory*, Addison Wesley Longman Limited, Harlow, 1996.
- [12] Sieros, G., Stamatis, A. and Mathioudakis, K. Jet engine component maps for performance modeling and diagnosis, *J Propuls Power*, 1997, **13**, (5), pp 665–674. DOI: [10.2514/2.5218](https://doi.org/10.2514/2.5218)
- [13] Kurzke, J. Advanced user-friendly gas turbine performance calculations on a personal computer, *Volume 5: Manufacturing Materials and Metallurgy; Ceramics; Structures and Dynamics; Controls, Diagnostics and Instrumentation; Education; IGTI Scholar Award*, American Society of Mechanical Engineers, 1995. DOI: [10.1115/95-GT-147](https://doi.org/10.1115/95-GT-147)
- [14] Mathioudakis, K., Politis, E. and Stamatis, A. A computer model as an educational tool for gas turbine performance, *Int J Mech Eng Educ*, 1999, **27**, (2), pp 113–125. DOI: [10.7227/IJMEE.27.2.3](https://doi.org/10.7227/IJMEE.27.2.3)
- [15] Baig, M.F., and Saravanamuttoo, H.I.H., “Off-design performance prediction of single-spool turbojets using gasdynamics,” *J Propuls Power*, 1997, **13**, (6), pp. 808–810. DOI: [10.2514/2.5240](https://doi.org/10.2514/2.5240)
- [16] Gasturb, G., *Gasturb Manual*, 2018. <https://www.gasturb.de/Downloads/Manuals/GasTurb13.pdf>
- [17] Davies, W.J., Hoelzer, C.A. and Vizzini, R.W. F-14 aircraft and propulsion control integration evaluation, *J Eng Power*, 1983, **105**, (3), pp 663–668. DOI: [10.1115/1.3227467](https://doi.org/10.1115/1.3227467)
- [18] Ohnabe, H., Masaki, S., Onozuka, M., Miyahara, K. and Sasa, T. Potential application of ceramic matrix composites to aero-engine components, *Compos Part A Appl Sci Manuf*, 1999, **30**, (4), pp 489–496. DOI: [10.1016/S1359-835X\(98\)00139-0](https://doi.org/10.1016/S1359-835X(98)00139-0)